BIMA Memo

A test of the homogeneous array concept using the Hat Creek array

David Wilner

30 December 1993

Abstract

In this memo, we review the three basic schemes of obtaining low spatial frequency data for millimeter array observations: (1) use of a large single dish, (2) interferometry with a multi-size array, and (3) scanning with a homogeneous array. We describe an application of the homogeneous array concept using the three antenna Hat Creek array. In an appendix, we analyze the effects of random, uncorrelated pointing errors on the effective interferometer primary beam shape, generalizing an analysis originally due to Rachel Padman and since lost. (This material is adapted from Chapter 4 of Wilner's thesis.)

1 Introduction

Large scale structure is poorly represented in images constructed from interferometer data because the finite size of the array antennas limits the range of observable spatial frequencies. The difficulty is exacerbated when attempting to image objects extended with respect to the interferometer primary beam, in particular star forming regions. This imaging problem is not simply solved by acquiring synthesis maps at several pointing centers, since a primary beam weighted average of the individual images still misses the low spatial frequency information that serves to connect the separate fields. Special effort is required to produce a better picture. Three basic schemes have been proposed: (1) use of a large single dish, (2) interferometry with a multi-size array, and (3) scanning with a homogeneous array. These methods were reviewed by Welch and Thornton (1984); here we update the status of application of these methods.

2 Methods

2.1 Large single dish

By imaging a source with a single dish, all Fourier components from 0 to $\pm D/\lambda$ are sampled, where D is the antenna diameter, with a weighting that depends on the antenna illumination. The short spacing information to complement a synthesis map may be more or less easily derived by Fourier transforming the single dish image and correcting for the antenna sensitivity function. This straightforward application of spatial frequency filtering is described in detail in the appendix to Vogel *et al.* (1984), who present the first use of this technique at millimeter wavelengths.

The essence of this method is that the single dish map is just the sky brightness convolved with the antenna sensitivity pattern, $T_B(x, y) * A(x, y)$, whose Fourier transform is given by the product $V(u, v)a(u, v)$, where $a(u, v)$ is the transform of $A(x, y)$. An estimate of the sensitivity pattern, $\hat{a}$, may be obtained from high signal-to-noise observations of a point source or a bright source with known structure, usually a planet. The short spacing information is then estimated by the division

$$\hat{V}(u, v) = \frac{[V(u, v)a(u, v)]}{\hat{a}(u, v)},$$

where conventional wisdom requires the single dish to be at least twice as large as the interferometer antennas in order to minimize the error in the antenna sensitivity pattern correction and to provide sufficient spatial frequency overlap to ensure accurate relative calibration of the two instruments.

The only significant shortcoming of this method is the need to use a large and accessible telescope. This is a serious restriction given the limited number of millimeter facilities and the investment in observing time required. The only viable single dish telescopes for three millimeter arrays comprised of 10–15 meter antennas are the Nobeyama 45 meter, IRAM 30 meter, and Onsala 20 meter telescopes, while at least two more options are available for the smaller 6 meter antennas that comprise the Hat Creek array, the NRAO 12 meter the FCRAO 14 meter telescopes. The larger telescopes also have more variable and less well defined illumination patterns, making the deconvolution process more difficult. Testimony to the difficulty is the small handful of examples of combined maps in the literature, of which only one is from an instrument other than the Hat Creek array (Mundy *et al.* 1988). As the interferometers expand to many elements and synthesized maps may be obtained in a single day, few astronomers will have the patience or inclination to complete the proposal and observing cycle at another telescope, which may take six months to a year or more, to gather short spacing information.

We note that a total power map made using a single array antenna just fills the gap from the origin of the (u, v) plane to the shortest spatial frequencies accessible to the interferometer. In practice, the sensitivity pattern is not sufficiently well known to bridge the entire spatial frequency gap, but data from one array antenna may significantly improve a synthesis map, if one is cautious with calibration.

2.2 Multi-size array

A separate array of smaller antennas may be used to obtain the short spatial frequency information by conventional interferometry. In this case, the size of the smaller array antennas should be 2–3 times smaller than the size of the larger array antennas. The shortest spacings may be obtained by total power mapping with one of the larger array antennas as described above. A first step in this direction was recently completed by Wright *et al.* (1993), who combined interferometric observations from the Hat Creek and Owens Valley arrays of the ^{13}CO J=1–0 line toward the nucleus of IC 342, thereby extending the spatial frequency coverage Owens Valley data made with 10 meter antennas to shorter spacings accessible to the 6 meter Hat Creek antennas. The principle disadvantage of this method is the requirement of a second complete interferometer.

A variant of this approach is to divide the illumination of the larger interferometer antennas into sub-apertures which may be individually cross correlated. This has the advantage of making the entire array self-contained, though at the expense of additional complexity in the receiver package and correlator. This technique has been tested with the Owens Valley interferometer, where the Nasmyth optics make it convenient to place two receivers that illuminate the antenna in two patchs

(Woody *et al.* 1991). To date, these attempts have suffered from a variety of technical problems, in particular false fringes caused by telescope emissions where the two beams overlap. While none of these problems are thought to be insurmountable, no complete maps have emerged from this effort.

2.3 Homogeneous array

The basis for this method was suggested by Ekers and Rots (1979). who pointed out that by scanning the interferometer across the source while cross correlating, it is possible to recover a range of spatial frequencies in the neighborhood of the nominal baseline using knowledge of the interferometer antenna sensitivity patterns. In particular, spacings shorter than a dish diameter may be obtained if the antennas are in close physical proximity. In this case, the measured visibilities are a function of the interferometer pointing direction (x_o, y_o) as well as the (u, v) point of the samples, and application of the Fourier transform with respect to x_o and y_o extends the range of measured visibilities away from (u, v) over the width of the of the transform of the antenna sensitivity pattern, i.e.

$$V(u, v; x_o, y_o) = \int T(x, y) A(x - x_o, y - y_o) \exp[-2\pi i(ux + vy)] dx dy$$

and

$$V(u - u_o, v - v_o) = \frac{\int V(u, v; x_o, y_o) \exp[2\pi i(u_o x_o + v_o y_o)] dx_o dy_o}{a(u_o, v_o)}$$

Spatial frequencies corresponding to about half the dish diameter may be recovered in this way. Fourier components from zero to about half the dish diameter may be obtained from a total power map from one of the array antennas, filling the entire central hole in (u, v) coverage.

This approach has recently received a great deal attention in the design stage of the proposed NRAO Millimeter Array (see NRAO Millimeter Array memo series). A variant of this method merges the derivation of the short spacings with the deconvolution phase of imaging in order to make the most use of the information at all pointing positions simultaneously (Cornwell 1988). Since the aperture plane sampling is limited at each pointing position, the deconvolution helps untangle the spatial frequency information in a process usually called "non-linear mosaicing". The Maximum Entropy Method (MEM) is used in the deconvolution step in reference to a methods such as CLEAN, which has well-known difficulties with smoothly varying large scale emission, the very structure of interest in this case. The MEM "default" image also provides an easy way to include *a priori* information to the procedure, for example a low resolution map of the source. Non-linear mosaicing has long been coded into the AIPS package task VTESS, and has been recently incorporated into Miriad by Bart Wakker (U. Illinois). The algorithm starts with a model estimate, multiplies the model by the primary beam pattern for each pointing, and convolves the result with the synthesized beam pattern for that pointing. Next, the χ^2 of the residuals from the observations at each pointing (and the total flux if not measured) are summed. MEM provides some constraints on the missing information in the form of the default map. Using standard minimization techniques, changes are found such that the model converges to a final state consistent with the data in all fields within the user specified noise parameter.

The principle advantage of the non-linear mosaicing method is that it requires no additional hardware. The technique was proven in concept by Cornwell (1988), who showed that a multiple pointing 20 cm VLA data set of the Simeis 57 supernova remnant successfully recovered spatial frequency information corresponding to about half the VLA antenna diameter by comparing with visibilities measured using the much smaller antennas of the DRAO synthesis telescope. Another test was performed by Uson and Cornwell (1991) using a multiple pointing 3.6 cm VLA observation of the Crab nebula and a total power map obtained with a VLBA antenna, although no comparison map was obtained to assess the results.

3 The Hat Creek interferometer as a homogeneous array

Here we describe an application of the homogeneous array concept using the Hat Creek millimeter array. For this test, we adopt the hybrid approach advocated by Braun (1988) and apply the nonlinear mosaic algorithm only on the shortest baselines. The reason for this restriction is that we are most interested in obtaining low spatial frequency information. The diameter of the array antennas is typically smaller than the sampling interval in the outer parts of the aperture plane, and the additional computational complexity required to involve multiple pointings from more extended configurations in the MEM solution results in little (if any) image improvement.

3.1 Observations

The test source was the very bright HCO^+ J=1–0 line emission at the Orion "radical position", part of the extended ridge of dense gas extending north of Orion-KL. The source center was $3\rlap{.}'5$ north and $0\rlap{.}'5$ east of Orion-KL. The data was acquired in four parts and consists of: (1) a large total power map using one of the array antennas; (2) a multi-pointing array observation in a compact configuration; (3) a full synthesis of the central field and (4) a comparison total power map made using the NRAO 12 meter telescope.

Antenna 3 of the Hat Creek array was used to obtain a well-sampled total power map of the region by position switching to an emission free position $30'$ west of the source. An 11×11 map with $1'$ grid spacing was obtained over the course of 04-05 April 1991. Since the total power observing mode was not well tested, several trials and software updates were required. The system gain stability was found to be adequate for total power mapping in very good weather conditions. Each grid point was observed a total of four times for 30 seconds, and after each integration a reference position at the map center was observed to check for pointing and gain drifts. The observing procedure was extremely conservative, and more than 30% of the data was discarded due to discrepancies. The absolute pointing was not checked during the observing procedure, but was assumed to be good to a better than $20''$ on the basis of pointing constants determined interferometrically. The beam size is about $2\rlap{.}'3$, and the correlator was configured to provide 256 channels over a 20 MHz bandwidth centered on the HCO^+ line. The line free regions of the spectra were fit with third order polynomials for baseline subtraction. One reason for the choice of test source was the narrow line emission (FWHM$\sim$ 2.3 km s^{-1}) at the grid center and over most of the mapped region, which gave more confidence in the baseline subtraction. Figure 1a shows the map of integrated emission spanning the velocity interval [8,12] km s^{-1}.

A six pointing synthesis map was obtained when the three array antennas were in the most compact configuration in August 1991. The pointing centers and half power beam widths are indicated in Figure 1a as dashed circles. The six pointing centers were each observed for 60 seconds in a sequence in order to minimize relative pointing and calibration errors at the expense of increased overhead in telescope motion. The interferometer gain and passband were calibrated in the usual way using observations of the quasars PKS 0420 and 3C 84. All shadowed data in which the primary beam of one antenna was partially blocked by another antenna was rejected. The correlator was configured for 64 channels over 5 MHz for the HCO^+ line. A full synthesis of the central field was obtained in the period June 1991 to January 1992 in a total of 9 configurations of the array with the identical setup.

The spatial frequencies sampled in the compact array configuration ranged from 1.8–2.7 kλ, with extensions around the nominal spacings corresponding to the 0.9 kλ antenna radius. Therefore, observations with the NRAO 12 meter telescope, which samples spatial frequencies out to 3.6 kλ, provides an excellent test of the success of the mosaicing process. The NRAO 12 meter telescope was used to map the central interferometer field on 29 March 1991. The source was mapped on on a 9×9 grid with $28''$ spacing following the procedure outlined for the S140 observations reported in Wilner and Welch (1994a). Figure 1b shows the map of integrated emission spanning the velocity interval [8,12] km s^{-1}.

3.2 Consistent calibration

Before proceeding with the non-linear mosaic procedure, we note that establishment of a consistent calibration scale is crucial for combination and comparison of the various data sets. Unfortunately, *consistent* calibration is not necessarily the same as *accurate* calibration. Model visibilities generated from the NRAO 12 meter maps after deconvolution with a $70''$ Gaussian beam were compared with the shortest baseline interferometer measurements. This implied a scale factor of $\sim$ 50 Jy/K T_R^* for the 12 meter data, which is not consistent with the theoretical gain of the 12 meter telescope (30 Jy/K T_R^*). However, the scaling is consistent with visibilities generated from the Antenna 3 maps, calibrated against the planet Jupiter, after deconvolution with a $2'.3$ Gaussian beam. The reason for the discrepancy is not clear. We adopt a calibration scale based on the Antenna 3 and interferometer data, and have multiplied the 12 meter maps by a constant factor for better agreement.

3.3 Non-linear mosaic

Holdaway (1990) presents an error analysis of non-linear mosaicing in the context of simulations of the proposed NRAO Millimeter Array, which shows that the most troublesome effects are introduced by interferometer pointing errors and poor knowledge of the antenna sensitivity pattern. It is encouraging that these effects are minor for the low dynamic range imaging attempted here. The effect of pointing errors is mitigated to some extent by restricting the data used to times where the rms tracking errors within individual 50 second integrations are less than $3''$, a quantity available in the data header. This constraint eliminated nearly 25% of the data, most of it in a short time range when the wind picked up. The effective primary beam of the interferometer is not well determined (see Wilner and Welch 1994a). We assumed a Gaussian shape, truncated at the 2% level, and left the FWHM as a parameter in mosaic process, exploring a range of values around the nominal $2'.3$ half power size.

The input to the mosaic procedure is a map and synthesized beam for each pointing center, characteristics of the primary beam, and an initial guess, a reference image, and noise estimate for the MEM algorithm. The Antenna 3 maps were deconvolved in the Fourier domain to produce an initial model of the large scale HCO^+ emission. This low resolution model was also used as the default image. The rms noise was estimated from off line channels. The algorithm converged in 5–18 iterations, with the number depending on the complexity of the emission in each channel. Examination of the residuals for each field generally showed best agreement for the central field, with larger differences apparent in the outer fields (where less redundant information is available). The procedure is sensitive to the adopted noise. Too low a value wrecks havoc as MEM begins to find structures that are not real and does not converge. Too high a value leads to almost no change in the default image and convergence in 2–3 iterations. Numerous empirical trials suggest acceptable values for the rms parameter lie in a relatively narrow range of about 25% of the nominal value, at least for this data set. The effective primary beam size did not have much effect on the final image, and similar results obtained for a range of sizes from $120''$–$140''$. However, care must be taken with the relative calibration since changing the beam size does affect the scaling of the initial model. Using a flat initial model with the correct total flux and the single dish default image in most cases worked as well as using the single dish model as the initial guess. However, the algorithm converged to a reasonable result only when the default image was specified, suggesting the *a priori* information contained in the single dish map may be critical for successful imaging.

3.4 Comparison with 12 meter maps

A comparison of the central spectrum of the Antenna 3 map with a spectrum derived from the NRAO maps convolved to the same $135''$ beam size shows deviations at only the 5% level after scaling to the peak. Therefore, the structure represented by the basic single dish data in the central field is consistent at low resolution.

How well did the non-linear mosaic procedure perform? Figure 2a–c shows the results for a 1 km s^{-1} wide velocity interval centered at v_{LSR}=11 km s^{-1}, a velocity range that contains extended emission as well as some interesting small scale structure. Figure 2a shows the single dish map obtained with Antenna 3, where the dots mark the locations of individual spectra, and the dashed circles show the half power beam widths for each of the six interferometer pointings. Figure 2b shows the output of the mosaic procedure after convolution with a $70''$ FWHM Gaussian beam. Examination of these images shows significant changes in detail in the higher resolution map, though the essential morphology of a north-south ridge with two peaks is maintained. Comparison with the map obtained with the NRAO 12 meter telescope illustrated in Figure 2c shows the extent to which these small scale features are believable. It is encouraging that the MEM mosaic and the high resolution single dish map show the same structures, though it is also apparent that the maps do not match perfectly. Part of the north-south elongation of the mosaic map may result from the poorer sensitivity of the interferometer data at these spatial frequencies associated with the source at low elevation. More importantly, the map morphologies disagree significantly toward the outer half power points of the individual pointing centers. The most extreme differences may be found near the southern edge of the maps, where the mosaic shows a brighter, more extended peak. This peak can also be identified as brighter and more extended in the Antenna 3 map used as the default, and so most of the disagreement is in the two total power maps rather than the mosaic procedure. Since this peak lies at the northern edge the Orion-KL source and becomes very much brighter just a fraction of a beam width farther south (see Figure 1), a relatively minor pointing error in the Antenna 3 map may be the major cause of the discrepancy.

Another comparison may be made in the Fourier domain. Figure 3 shows annular averages of the visibilities for the central interferometer field from three data sets, in bins of 4 nanosecond width. The circles show visibilities derived from the NRAO 12 meter map, the squares show visibilities derived from the MEM mosaic model, and the triangles show the visibilities obtained directly with the interferometer. One should keep in mind that the 12 meter data was scaled to match the interferometer and Antenna 3 data before application of the mosaicing procedure, so the apparent good agreement in this Figure is a somewhat misleading. However, the mosaic algorithm does generate accurate Fourier components that bridge the gap between the Antenna 3 map and the shortest interferometer baselines, and in this sense the test of the procedure was very successful. For this source, it is clear that the addition of single dish data is very important as the visibility amplitude measured by the interferometer represents only a small fraction of the total flux. If this method is to be used routinely at Hat Creek, then extra care will have to be taken to ensure consistent calibration and excellent pointing in single antenna total power maps. Simulations of realistic observing conditions should be performed to quantify the requirements for the present six element array.

Finally, visibilities were derived from the non-linear mosaic model and combined with the full synthesis data set to make high resolution maps of the central field with full spatial frequency coverage. Figure 4 shows a series of channel maps obtained from Maximum Entropy deconvolution of the synthesized maps, convolved with a $9'' \times 6''$ Gaussian beam. The astrophysical interpretation of this data will be given elsewhere (Wilner and Welch 1994b).

4 Concluding Remarks

The HCO^+ J=1–0 emission from the OMC-N region demonstrates that the homogeneous array technique has promise for routine use with the Hat Creek interferometer. In this example, the information in the total power map obtained with a single array antenna provided most of the total flux and proved crucial for the convergence of the non-linear mosaic algorithm. If typical, then it will be prudent to equip as many antennas as possible in the expanded array with the single dish capability so that the data can be acquired quickly for inclusion in the imaging process.

A Uncorrelated pointing errors and primary beam shape

In this appendix, we analyze the effects of random, uncorrelated pointing errors on the effective interferometer primary beam shape, generalizing an analysis originally due to Rachel Padman and since lost. Observers should be aware of these effects when performing data processing tasks that depend on an estimate the primary beam shape, for example mosaicing, or deriving a model of large scale structure from a single dish map.

A.1 Pointing Errors

Real interferometer antennas, particularly the older millimeter wave antennas at Hat Creek, do not point and track astronomical sources perfectly. The associated errors occur on all timescales, from rapid fluctuations within a single visibility sample to antenna mispointings that persist throughout an entire synthesis track. Here we restrict attention to *rapid, uncorrelated* pointing errors between two antennas, where we more carefully specify the meaning of these below. Such errors may arise from wind buffeting the antennas, or from the settling of the antennas cycling among multiple fields, or noisy encoders.

A.2 Gaussian beams

To simplify the mathematics, we assume Gaussian beam patterns for the antennas,

$$A_i(x,y) = G_i \exp\left[-\alpha_i^2(x^2+y^2)\right]$$

where

$$\alpha_m^2 = \frac{1}{2\sigma_{B,i}^2} = \frac{4\ln 2}{\theta_{1/2,i}^2}.$$

In the absence of pointing errors, the effective beam for the antenna pair (i,j) is the geometric mean of the two antenna beams

$$\begin{aligned} A_{eff}(x,y) &= \sqrt{A_i(x,y)A_j(x,y)} \\ &= \left\{G_i \exp\left[-\alpha_i^2(x^2+y^2)\right] G_j \exp\left[-\alpha_j^2(x^2+y^2)\right]\right\}^{1/2}. \end{aligned}$$

Now introduce pointing errors into each antenna such that

$$\begin{aligned} A(x,y) &= \{A_i(x-x_i, y-y_i)A_j(x-x_j, y-y_j)\}^{1/2} \\ &= \left\{G_i \exp\left[-\alpha_i^2((x-x_i)^2+(y-y_i)^2)\right] G_j \exp\left[-\alpha_j^2((x-x_j)^2+(y-y_j)^2)\right]\right\}^{1/2} \\ &= \left\{G_i \exp\left[-\alpha_i^2(x^2+y^2)\right] G_j \exp\left[-\alpha_j^2(x^2+y^2)\right]\right\}^{1/2} \times \\ &\quad \left\{\exp\left[-\alpha_i^2(-2xx_i+x_i^2-2yy_i+y_i^2)-\alpha_j^2(-2xx_j+x_j^2-2yy_j+y_j^2)\right]\right\}^{1/2} \\ &= A_{eff}(x,y) \times \mathcal{C}(x,y,x_i,y_i,x_j,y_j,\alpha_i^2,\alpha_j^2). \end{aligned}$$

where $\mathcal{C}(x,y,x_i,y_i,x_j,y_j,\alpha_i^2,\alpha_j^2)$ is a multiplicative factor on $A_{eff}(x,y)$ that depends on the pointing errors, the beam sizes and source position. We need only evaluate the C factor under specific assumptions about the pointing errors to determine the distortion to the nominal beam shape.

A.3 Random Gaussian errors

One way to proceed is to assume the pointing errors in each coordinate for each antenna x_i, x_j, y_i, y_j have identical Gaussian distributions. Other functional forms that may approximate more closely the actual pointing error behavior should also be considered, for example a uniform distribution to represent an antenna flopping between gear teeth. Here we restrict attention to Gaussian distributions, i.e.

$$p(x_i) = \frac{\beta}{\sqrt{\pi}} \exp\left[-\beta^2 x_i^2\right], \quad \text{where } \beta^2 = \frac{1}{2\sigma_P^2}$$

where σ_P is the rms pointing error. We further assume the pointing errors in each coordinate for each antenna are mutually independent, or uncorrelated, and note this may not be a very realistic assumption. In this case, the true beam– corrected for the pointing errors– and properly normalized, is given by

$$A_p(x,y) = A_{eff}(x,y) \times \frac{<\mathcal{C}(x,y)>}{<\mathcal{C}(0,0)>} \tag{1}$$

where the angle brackets denote a time average. For the time average to be meaningful, we must also make the important assumption that changes in x_i, x_j, y_i, y_j are much faster than changes in the visibility function sampling.

What is the appropriate timescale in this time average? Since the sky is convolved by the interferometer primary beam, samples should be made at least twice in the time it takes the baseline to change by the equivalent of a dish diameter. For antennas with diameter D and a baseline with length b, an upper limit to the sampling interval is

$$\Delta t = \left(\frac{1}{2}\right)\left(\frac{12}{\pi}\right)\left(\frac{D}{b}\right) \text{ hours} = 412\left(\frac{D}{6 \text{ m}}\right)\left(\frac{100 \text{ m}}{b}\right) \text{ seconds}$$

Thus we require the correction factor to have a well defined expectation value in a time interval on the order of a few minutes. One may think of this as randomly waving the antenna primary beams over the source during the course of one integration.

The time average of $\mathcal{C}(x, y)$ is

$$\begin{aligned} < \mathcal{C}(x,y) > &= \left\{ \int_{-\infty}^{\infty}\int_{-\infty}^{\infty}\int_{-\infty}^{\infty}\int_{-\infty}^{\infty} \exp\left[-\alpha_i^2(-2xx_i + x_i^2 - 2yy_i + y_i^2)\right.\right. \\ &\quad \left.\left. -\alpha_j^2(-2xx_j + x_j^2 - 2yy_j + y_j^2)\right] [p(x_i)p(x_j)p(y_i)p(y_j)]\, dx_i dx_j dy_i dy_j \right\}^{1/2} \\ &= \left\{ \int_{-\infty}^{\infty} \exp\left[-\alpha_i^2 x_i^2 + 2\alpha_i^2 x x_i\right] p(x_i)dx_i \int_{-\infty}^{\infty} \exp\left[-\alpha_i^2 y_i^2 + 2\alpha_i^2 y y_i\right] p(y_i)dy_i \;\times \right. \\ &\quad \left. \int_{-\infty}^{\infty} \exp\left[-\alpha_j^2 x_j^2 + 2\alpha_j^2 x x_j\right] p(x_j)dx_j \int_{-\infty}^{\infty} \exp\left[-\alpha_j^2 y_j^2 + 2\alpha_j^2 y y_j\right] p(y_j)dy_j \right\}^{1/2}. \end{aligned}$$

The four integrals in this expression are very similar, and for the moment we consider just the first one, I_1. Substituting for $p(x_i)$ gives

$$I_1 = \frac{\beta}{\sqrt{\pi}} \int_{-\infty}^{\infty} \exp\left[2\alpha_i^2 x x_i - (\alpha_i^2 + \beta^2)x_i^2\right] dx_i$$

which we can integrate using

$$\begin{aligned} I_2 &= \int_0^{\infty} \exp\left[-(at^2 + bt + c)\right] dt \\ &= \frac{1}{2}\sqrt{\frac{\pi}{a}} \exp\left[\frac{b^2 - ac}{a}\right]\left[1 - \text{erf}\left(\frac{b}{\sqrt{a}}\right)\right] \end{aligned}$$

from Abramowitz and Stegan p. 302. Although I_2 differs from I_1 in the limits of integration, we can (fortunately) make use of symmetry to determine I_1 from I_2 since

$$\int_{-\infty}^{\infty} = \int_{-\infty}^{0} + \int_0^{\infty}$$

and, in this case,

$$\int_{-\infty}^{0} f(x_i)dx_i = -\int_0^{-\infty} f(x_i)dx_i = \int_0^{\infty} f(-x_i)d(-x_i).$$

Identifying the constants, we find

$$\begin{aligned} I_2 &= \int_0^{\infty} \exp\left[-\alpha_i^2 x_i^2 + 2\alpha_i^2 x x_i\right] \frac{\beta}{\sqrt{\pi}} \exp\left[-\beta^2 x_i^2\right] dx_i \\ &= \frac{\beta}{\sqrt{\pi}}\sqrt{\frac{\pi}{4(\alpha_i^2 + \beta^2)}} \exp\left[\frac{\alpha_i^4 x^2}{(\alpha_i^2 + \beta^2)}\right]\left[1 - \text{erf}\left(\frac{-\alpha_i^2 x}{2(\alpha_i^2 + \beta^2)}\right)\right] \end{aligned}$$

and

$$I_1 = \frac{\beta}{\sqrt{\pi}}\sqrt{\frac{\pi}{4(\alpha_i^2+\beta^2)}}\exp\left[\frac{\alpha_i^4 x^2}{(\alpha_i^2+\beta^2)}\right][2].$$

Finding analogous expressions for the other three integrals and collecting terms, we get

$$\begin{aligned} < \mathcal{C}(x,y) > \; = \; & \beta^2 \left\{ \left[\frac{1}{(\alpha_i^2+\beta^2)}\right]\exp\left[\frac{\alpha_i^4 x^2}{(\alpha_i^2+\beta^2)}\right] \times \left[\frac{1}{(\alpha_i^2+\beta^2)}\right]\exp\left[\frac{\alpha_i^4 y^2}{(\alpha_i^2+\beta^2)}\right] \times \right. \\ & \left. \left[\frac{1}{(\alpha_j^2+\beta^2)}\right]\exp\left[\frac{\alpha_j^4 x^2}{(\alpha_j^2+\beta^2)}\right] \times \left[\frac{1}{(\alpha_j^2+\beta^2)}\right]\exp\left[\frac{\alpha_j^4 y^2}{(\alpha_j^2+\beta^2)}\right]\right\}^{1/2} \qquad (2) \end{aligned}$$

To make further progress, we consider the the usual situation where the antennas i and j are identical, i.e.

$$\alpha_i = \alpha_j = \alpha.$$

With this simplification, equation (2) reduces to

$$< \mathcal{C}(x,y) > \; = \left[\frac{\beta^2}{(\alpha^2+\beta^2)}\right]\exp\left[(x^2+y^2)\left(\frac{\alpha^4}{\alpha^2+\beta^2}\right)\right],$$

and the "pointing corrected primary beam" is

$$\begin{aligned} A_p(x,y) &= G\exp[-\alpha^2(x^2+y^2)] \times \exp\left[(x^2+y^2)\left(\frac{\alpha^4}{\alpha^2+\beta^2}\right)\right] \\ &= G\exp\left[-(x^2+y^2)\left(\frac{\alpha^2\beta^2}{\alpha^2+\beta^2}\right)\right] \\ &= G\exp\left[-\frac{(x^2+y^2)}{2(\sigma_B^2+\sigma_P^2)}\right]. \qquad (3) \end{aligned}$$

Equation (3) highlights the intuitively appealing result that the Gaussian beam size is effectively broadened by the addition (in quadrature) of the rms pointing errors.

References

Braun, R. 1988, NRAO Millimeter Array Memo No. 54.

Cornwell, T.J. 1988, A&A, 202, 316.

Cornwell, T.J. 1989, in *Synthesis Imaging in Astronomy*, Astronomical Society of the Pacific Conference Series, vol. 6, eds. Perley, R.A., Schwab, F.R. and Bridle, A.H. (San Francisco: ASP), p. 277.

Ekers, R.D. and Rots, A.H. 1979, in *Image Formation from Coherence Functions in Astronomy*, ed. van Schooneveld, C. (Dordrecht:Reidel), p. 61.

Holdaway, M. 1990, NRAO Millimeter Array Memo No. 61.

Mundy, L.G., Cornwell, T.J., Masson, C.R., Scoville, N.Z., Baath, L.B. and Johansson, L.E.B. 1988, ApJ, 325, 382.

Uson, J.M. and Cornwell, T.J. 1991, in *Radio Interferometry: Theory, Techniques and Applications*, Astronomical Society of the Pacific Conference Series, vol. 19, eds. Perley, R.A. and Cornwell, T.J. (San Francisco: ASP), p. 260.

Vogel, S.N., Wright, M.C.H., Plambeck, R.L. and Welch. W.J. 1984, ApJ, 283, 655.

Welch, W.J. and Thornton, D.D. 1984, in *International Symposium on Millimeter and Submillimeter Wave Radio Astronomy*, (Granada:URSI), p. 53.

Wilner, D.J. and Welch, W.J. 1994a, Ap.J. in press.

Wilner, D.J. and Welch, W.J. 1994b, in preparation.

Woody, D.P., Scoville, N.Z., and Mundy, L.G. 1991, in *Radio Interferometry: Theory, Techniques and Applications*, Astronomical Society of the Pacific Conference Series, vol. 19, eds. Perley, R.A. and Cornwell, T.J. (San Francisco: ASP), p. 81.

Wright, M.C.H., Ishizuki, S., Turner, J.L., Ho, P.T.P. and Lo, K.Y. 1993, ApJ, 406, 470.

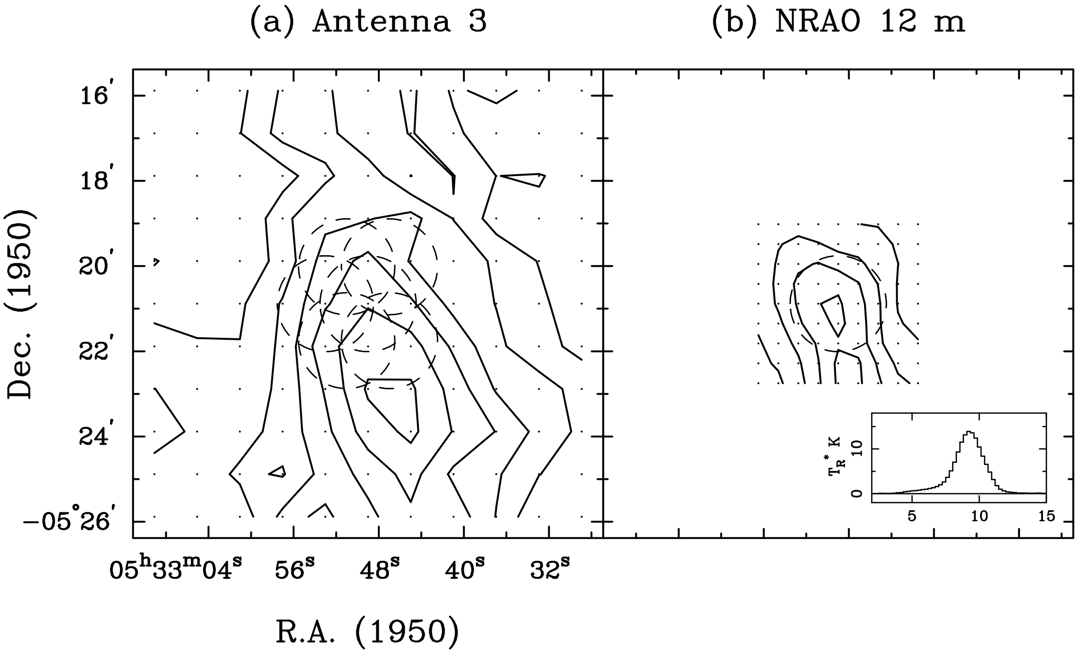

Figure 1: (a) Map of the HCO^+ J=1–0 integrated intensity spanning the velocity interval [8,12] km s^{-1}made with one antenna of the Hat Creek array. The beam size is $\sim 135''$, and the lowest contour and contour interval are 180 Jy/beam. Dots mark the locations of individual spectra. The six dashed circles indicate the half power primary beam widths of the interferometer pointing centers used in the non-linear mosaic procedure. (b) Same as (a), but from the NRAO 12 meter telescope. The beam size is $70''$, and the lowest contour and contour interval are 100 Jy/beam. The dashed circle indicates the half power primary beam width of the central interferometer field. The inset in the lower right shows the spectrum with a $135''$ FWHM beam.

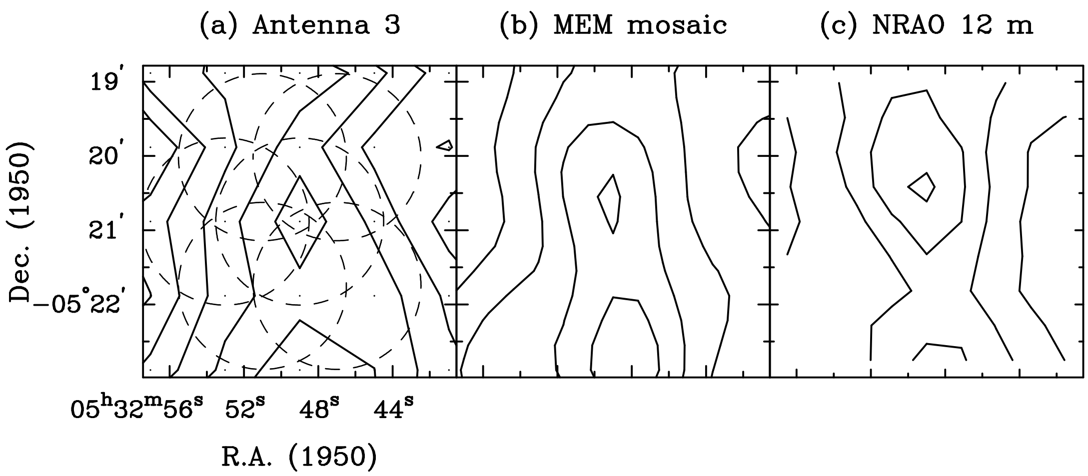

Figure 2: Example of the non-linear mosaic procedure. All maps span the velocity interval [10.5,11.5] km s^{-1}. (a) Map from Antenna 3. The symbols are the same as in Figure 1. The lowest contour and contour interval are 100 Jy/beam. (b) Result of the non-linear mosaic using the Antenna 3 map and the six pointing interferometer data set from the most compact antenna configuration. The Maximum Entropy model has been convolved with a $70''$ gaussion. The lowest contour and contour interval are 68 Jy/beam. (c) Map from the NRAO 12 meter telescope, which has the same beam size and contours as the map in panel (b).

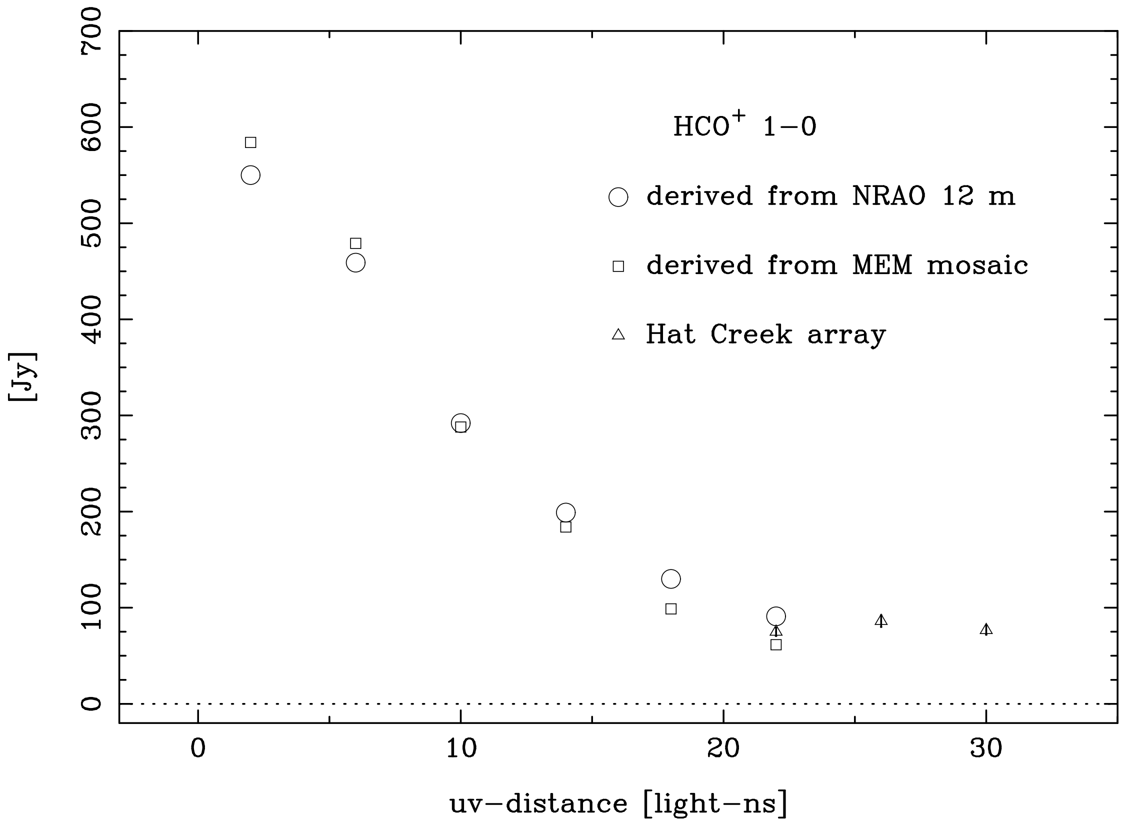

Figure 3: Amplitudes of the HCO^+ J=1–0 visibilities in the velocity range [10.5,11.5] km s^{-1}, corresponding to Figure 2, vector averaged in concentric annuli in the (u, v) plane. Data points derived from the NRAO 12 meter map are indicated by circles, those obtiained with the Hat Creek array by triangles, and those derived from the non-linear mosaic process by squares. Note that ten light-nanoseconds corresponds to 0.89 kλ. The statistical errors are smaller than the symbol size. An arbitrary scaling has been applied to the 12 meter data (see text), so that only the shape defined by the 12 meter data points is relevant.

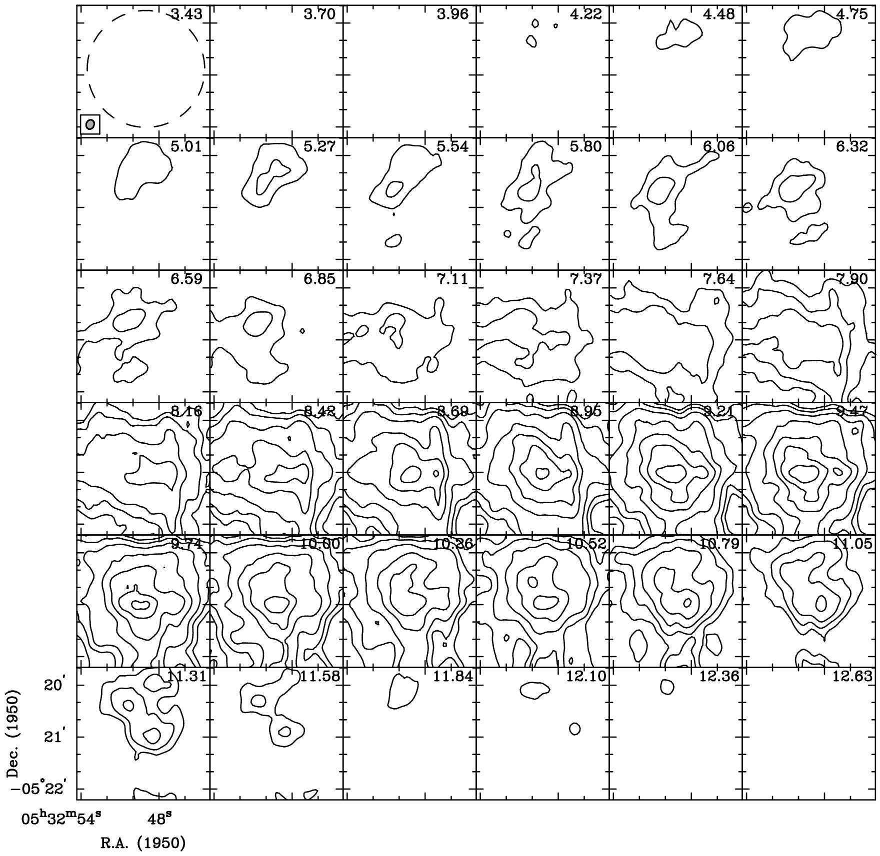

Figure 4: Channel maps for the full synthesis of the central field. The contours are $(1, 2, 4, 8, 12, 16, 20, 24, 28) \times 1.2$ Jy/beam (2σ). The $9'' \times 6''$ synthesized beam is illustrated in the lower left corner of the first panel. A dashed circle shows the interferometer primary beam half power point.